



Letter

# Assessment of Anthropogenic Methane Emissions over Large Regions Based on GOSAT Observations and High Resolution Transport Modeling

Rajesh Janardanan <sup>1,2,\*</sup>, Shamil Maksyutov <sup>1,2</sup> , Akihiko Ito <sup>1</sup>, Yoshida Yukio <sup>1,2</sup>   
and Tsuneo Matsunaga <sup>1,2</sup>

<sup>1</sup> Center for Global Environmental Research, National Institute for Environmental Studies, 16-2 Onogawa, Tsukuba 305-8506, Japan; shamil@nies.go.jp (S.M.); itoh@nies.go.jp (A.I.); yoshida.yukio@nies.go.jp (Y.Y.); matsunag@nies.go.jp (T.M.)

<sup>2</sup> Satellite Observation Center, National Institute for Environmental Studies, 16-2 Onogawa, Tsukuba 305-8506, Japan

\* Correspondence: rajesh.janardanan@nies.go.jp; Tel.: +81-29-850-2968

Received: 10 August 2017; Accepted: 8 September 2017; Published: 11 September 2017

**Abstract:** Methane is an important greenhouse gas due to its high warming potential. While quantifying anthropogenic methane emissions is important for evaluation measures applied for climate change mitigation, large emission uncertainties still exist for many source categories. To evaluate anthropogenic methane emission inventory in various regions over the globe, we extract emission signatures from column-average methane observations ( $XCH_4$ ) by GOSAT (Greenhouse gases Observing SATellite) satellite using high-resolution atmospheric transport model simulations.  $XCH_4$  abundance due to anthropogenic emissions is estimated as the difference between polluted observations from surrounding cleaner observations. Here, reduction of observation error, which is large compared to local abundance, is achieved by binning the observations over large region according to model-simulated enhancements. We found that the local enhancements observed by GOSAT scale linearly with inventory based simulations of  $XCH_4$  for the globe, East Asia and North America. Weighted linear regression of observation derived and inventory-based  $XCH_4$  anomalies was carried out to find a scale factor by which the inventory agrees with the observations. Over East Asia, the observed enhancements are 30% lower than suggested by emission inventory, implying a potential overestimation in the inventory. On the contrary, in North America, the observations are approximately 28% higher than model predictions, indicating an underestimation in emission inventory. Our results concur with several recent studies using other analysis methodologies, and thus confirm that satellite observations provide an additional tool for bottom-up emission inventory verification.

**Keywords:** methane emission inventory; GOSAT  $XCH_4$ ; Lagrangian model; greenhouse gases; anthropogenic emission

## 1. Introduction

Atmospheric methane ( $CH_4$ ) is an important anthropogenic greenhouse gas which contributes about 20% of the total radiative forcing from greenhouse gases, second only to carbon dioxide ( $CO_2$ ) [1]. Methane is released to the atmosphere by both natural and anthropogenic sources, and is depleted by oxidation with hydroxyl radical (OH) in the troposphere, oxidation with drier soil and by photolysis in the stratosphere. Anthropogenic emission contributes approximately 50–65% of the global methane budget [2]. Due to the large radiative forcing, reducing anthropogenic  $CH_4$  emission is important for mitigation of potential impact of global warming (e.g., [3]). The atmospheric  $CH_4$  level has

drastically increased since the industrial revolution [4], and its growth rate exhibits large interannual variability over recent few decades [5], the causes of which are not fully understood on a global scale (e.g., [2,5,6]). In addition, in the context of recent slowdown in global warming, atmospheric methane variability and the anthropogenic contribution to this variability is particularly important [7,8]. Recent studies [9,10] indicated the plausible causes (such as decline in OH radicals or increase in biogenic emissions) of renewed growth rate in the past decade. On regional spatial scales, CH<sub>4</sub> emission estimates from bottom-up and top-down approaches differ considerably (e.g., [11–15]). Bottom-up emission inventories often have large uncertainties owing to the uncertainties in the information on source intensity, activity and other statistical data. For example, Karion et al. [16] have found through aircraft observations that EPA (United States Environmental Protection Agency) and EDGAR (Emission Database for Global Atmospheric Research) underestimate the CH<sub>4</sub> emissions from oil and natural gas sector in their analysis on a spatial scale of few hundred kilometers over southern United States. Similarly, differences between EPA and EDGAR in various emission sectors are discussed in Maasakkers et al. [17]. Turner et al. [18] applied a 50 km resolution inverse model utilizing GOSAT data over North America to conclude that EPA emission inventory is underestimating emissions by some sectors. Further, since the emission of methane from anthropogenic sources are highly variable within same source category, the quantification is much more difficult than anthropogenic emission of CO<sub>2</sub> which are deduced from better known fuel use data.

In the past decades, studies on the atmospheric CH<sub>4</sub> variability and the inverse estimation of CH<sub>4</sub> flux were mainly based on ground-based measurements and data from aircraft and ship observations (e.g., [12,19,20]). Since the surface measurement network of CH<sub>4</sub> is sparse, satellite observations have been extensively used to understand the variations of atmospheric CH<sub>4</sub> associated with intense local activities (e.g., [21]) due to the advantage of their large spatial and temporal coverage. Among them, the Greenhouse gases Observing SATellite (GOSAT) has been providing column-averaged dry-air mole fractions of atmospheric CH<sub>4</sub> (XCH<sub>4</sub>) since its launch in 2009 [22]. GOSAT is a joint mission of the Japanese Ministry of the Environment (MOE), the Japan Aerospace Exploration Agency (JAXA) and the National Institute for Environmental Studies (NIES). XCH<sub>4</sub> is retrieved from the Short-Wavelength InfraRed (SWIR) solar spectra observed by Thermal And Near infrared Sensor for carbon Observation–Fourier Transform Spectrometer (TANSO–FTS) instrument [22,23] with a single scan accuracy of more than 2% at 100–1000 km spatial resolution [24].

Considering the sparsity of the ground-based observation networks and the necessity for wide spatial and temporal coverage, satellite observations such as from GOSAT can be an additional or alternative tool for estimation and monitoring of anthropogenic greenhouse gas emissions (e.g., [25–29]) by emission hotspots such as megacities and power plants and other intensive sources such as biomass burning [21,30]. Therefore, there is an emerging interest in the use of space-based observation of greenhouse gases for estimation and verification of their emissions. Here in this paper, we report an analysis method using GOSAT satellite observation of XCH<sub>4</sub> and a high-resolution atmospheric transport model to derive local anthropogenic abundance from GOSAT observation and EDGAR emission inventory, and to statistically model the agreement between them.

## 2. Data

### 2.1. GOSAT XCH<sub>4</sub> Observations

This study utilized the National Institute for Environmental Studies GOSAT Short Wavelength InfraRed XCH<sub>4</sub> Level 2 product (NIES SWIR L2 v02.21) during a period of June 2009 to December 2012. The retrieved XCH<sub>4</sub> data have been validated using XCH<sub>4</sub> observations at selected Total Column Carbon Observation Network (TCCON) sites and reported to have mean bias of −5.9 ppb and mean standard deviation of 12.6 ppb [20]. The data processing and related information can be found in GOSAT Data Archive Service (GDAS) website, <https://data2.gosat.nies.go.jp/>.

## 2.2. CH<sub>4</sub> Emission Inventory

For the high-resolution transport modeling, the CH<sub>4</sub> emission data used are the anthropogenic emission inventory (Emission Database for Global Atmospheric Research (EDGAR) v4.2 FT2010 [31], for the period 2009–2010 at 0.1° resolution. For the years 2011 and 2012, the data are scaled using the global total value of those years as reported by EDGAR. This scaling is justified better for global analysis because it is supposed to improve representing the emissions for those years instead of using emission for 2010 for other years. To check the effect of scaling, we have compared the emission in 2010 with that prepared by scaling data for 2009 (Figure S3). The sectors considered in the EDGAR database are: energy use, industrial processes, solvents, agriculture and waste. The anthropogenic emissions did not include forest/peat fire. To account for the contribution from wetland emission and soil sink of methane, model simulated values were adjusted in the observations. For this, we used fluxes from Vegetation Integrative Simulator for Trace gases model (VISIT) [32].

## 2.3. Meteorological Data Used for Transport Simulations

The meteorological data used for the Lagrangian transport simulation are from Japanese Meteorological Agency (JMA) Climate Data Assimilation System (JCDAS) [33]. The required parameters, such as three-dimensional wind fields, temperature and humidity, were provided at  $1.25 \times 1.25^\circ$  spatial resolution and 40 vertical hybrid sigma-pressure levels and the temporal resolution of input is 6 h.

## 3. Methods

The method is similar to estimating anthropogenic emission signature in GOSAT XCO<sub>2</sub> due to Large Point Sources proposed by Janardanan et al. [26]. This study utilizes a Lagrangian Particle Dispersion Model, FLEXPART [34,35] with EDGAR anthropogenic methane emission inventory (spatial resolution  $0.1 \times 0.1^\circ$ ) to simulate (see Section 3.1) XCH<sub>4</sub> abundance ( $\Delta\text{XCH}_{4,\text{sim}}$ ) caused by local anthropogenic emissions at all GOSAT satellite observation locations with valid retrieval data. Spatial resolution of the emission inventory and the tracer transport simulations are selected to be approximately at the size of GOSAT surface observation footprint of about 10 km, to avoid loss of information due to spatial smoothing by transport model. We then subtract from the observations the influence due to wetland emissions and sink in the soil using model simulated values. Based on the model estimates of XCH<sub>4</sub> abundance, we separate satellite observations as substantially influenced by anthropogenic emissions ( $\Delta\text{XCH}_{4,\text{sim}} > 1$  ppb) and those from relatively cleaner background ( $\Delta\text{XCH}_{4,\text{sim}} < 1$  ppb). Observed enhancements ( $\Delta\text{XCH}_{4,\text{obs}}$ ) were computed as difference of observations from polluted regions from the regional background, which is defined as the monthly average of observations with low ( $\Delta\text{XCH}_{4,\text{sim}} < 1$  ppb) simulated contribution from anthropogenic sources in each  $10 \times 10^\circ$  region (see Section 3.2). To reduce the stochastic errors associated with each satellite observation, we average the observed ( $\Delta\text{XCH}_{4,\text{obs}}$ ) and simulated XCH<sub>4</sub> ( $\Delta\text{XCH}_{4,\text{sim}}$ ) anomalies into 2 ppb bins depending on simulated values. Thus the single scan random error can be reduced proportional to the inverse square root of the number of observations averaged in that bin (see supplementary information). To find how well the observed enhancements agree with the anthropogenic CH<sub>4</sub> emission inventory, we perform a weighted linear regression, BLUE estimator (best linear unbiased estimator) (with weightage inversely proportional to the standard error in mean  $\Delta\text{XCH}_{4,\text{obs}}$  in each bin [36]) with observed XCH<sub>4</sub> abundance as dependent variable and simulated enhancements as independent variable. The upper limit of 20 ppb in regression analysis is to avoid bins with large standard error in the average  $\Delta\text{XCH}_{4,\text{obs}}$ , due to the diminishing number of observations. Most of the observations having high contribution from anthropogenic sources come within this upper limit. The regression coefficient (slope value) thus obtained indicates the factor by which the observations compare with the inventory-based estimates.

### 3.1. Atmospheric CH<sub>4</sub> Transport Simulation

We calculated the fraction of XCH<sub>4</sub> due to the anthropogenic emissions for all GOSAT observations for a period from June 2009 until December 2012 using FLEXPART and EDGAR emissions. In this, 10,000 particles were released from the geographic locations of GOSAT observations and transported two days with the time inverted three-dimensional wind fields. The meteorological input to the model was from JCDAS [33] reanalysis. The time integral of particle density below the mixing height in an emission grid cell gives the sensitivity of the XCH<sub>4</sub> at the observation location to the emission in that grid [37]. The area integral of the emission sensitivity corresponding to an observation multiplied by the CH<sub>4</sub> flux gives the XCH<sub>4</sub> at the observation location [38]. To correct for the influence of natural fluxes on XCH<sub>4</sub>, we simulated FLEXPART in the same way. The simulated values were then subtracted from the GOSAT observations (XCH<sub>4,cor</sub> in Equation (1)) before any analysis is carried out.

### 3.2. Correction for Terrain Related Bias in XCH<sub>4</sub>

As methane is removed from the troposphere due to reaction with OH radicals and depletion in the stratosphere, and its concentration in stratosphere is low due to long residence time [39], the contribution of stratospheric fraction to the total column methane becomes important and causes lowering of XCH<sub>4</sub> over high terrains [25]. To remove the influence of terrain height on XCH<sub>4</sub>, we establish a quadratic polynomial regression between terrain height and XCH<sub>4</sub> in each region (Figure S1). This fit is subtracted from the XCH<sub>4</sub> data to compensate for influence of terrain height on analysed XCH<sub>4</sub> data.

### 3.3. ΔXCH<sub>4</sub> from GOSAT

GOSAT XCH<sub>4</sub> observations (in ppb) are used for estimating the XCH<sub>4</sub> enhancements due to anthropogenic emissions (ΔXCH<sub>4,obs</sub>) relative to observations in surrounding cleaner areas. For this, we consider the observations where model simulated enhancements due to anthropogenic emissions (ΔXCH<sub>4,sim</sub>) exceed 1 ppb to have anthropogenic CH<sub>4</sub> emission signature, and the rest of the observations as clean background observations. As a first step, we remove the terrain related bias in XCH<sub>4</sub> and we subtract the fractional influence of natural fluxes on XCH<sub>4</sub> (influence of wetland emission and soil sink) by subtracting the model-simulated values (with natural fluxes) from the observations (corrected value designated as XCH<sub>4,cor</sub>). The XCH<sub>4</sub> enhancement relative to the clean surrounding observations is calculated as the difference between corrected observations and a clean background value XCH<sub>4,bg</sub>.

$$\Delta XCH_{4,obs} = XCH_{4,cor} - XCH_{4,bg} \quad (1)$$

To calculate the background mixing ratios, XCH<sub>4,bg</sub>, we defined regions of 10 × 10° globally and estimated the monthly means of corrected observations (XCH<sub>4,cor</sub>) for locations corresponding to simulated XCH<sub>4</sub> abundance, ΔXCH<sub>4,sim</sub> < 1 ppb (when there are at least 10 clean observations in a region) in each region. To overcome the limitation of random error associated with GOSAT observation and for fitting a regression between observed enhancements (ΔXCH<sub>4,obs</sub>) and the simulated enhancements (ΔXCH<sub>4,sim</sub>), we aggregated all paired values into 2 ppb bins based on simulated values of ΔXCH<sub>4,sim</sub>. Resulting data are used in regression analysis.

## 4. Results and Discussion

Unlike CO<sub>2</sub>, methane has no strong localized sources such as power plants, thus strongest emissions are concentrated in urban regions, irrigated agricultural lands and regions of high livestock density. While the strong diurnally varying CO<sub>2</sub> fluxes from photosynthesis are disturbing the CO<sub>2</sub> field, there is no such strong short-term variability in CH<sub>4</sub> emissions. Our results show large number of simulated and observed enhancements in the range of 10 to 20 ppb globally. A linear relationship between observed and simulated enhancements can be reliably established in the range of 1–20 ppb

(more than the ~12.6 ppb random error of GOSAT XCH<sub>4</sub> [23]), while, for GOSAT XCO<sub>2</sub>, the range is 0–1 ppm (as discussed in Janardanan et al., 2016 [26]), which is half of the single scan random error of 2 ppm XCO<sub>2</sub>. Thus, compared to CO<sub>2</sub>, detectable CH<sub>4</sub> abundance due to anthropogenic sources are more robust.

The inventory based XCH<sub>4</sub> anomalies as simulated by the Lagrangian transport model revealed many emission hotspot regions all over the globe. These include northern part of Europe, Middle East, northwest and northeast India and Southeast Asia and China. Significant XCH<sub>4</sub> abundance is also seen over California, Mexico City and eastern parts of the United states (Figure 1). Over East Asia, the high XCH<sub>4</sub> anomalies are found over central and southeastern provinces of China, where the major emission source is rice paddy [40]. In northeastern provinces, having intense livestock and coal mining [41], the XCH<sub>4</sub> anomalies are high (10–20 ppb in 2° averages). In India, high signals are seen over northeastern parts, which correspond to large scale animal agriculture in that region [42]. In addition, northwestern and northeastern India, having rice paddy fields, show high anomalies in the 2° averages pictures. The locations of high concentrations also coincide with high livestock density (e.g., [43,44]). Middle East, Saudi Arabia, Egypt, Iran, etc. showed high XCH<sub>4</sub> abundance, possibly due to the oil and natural gas exploration in those regions. The region in tropical Africa, where we get high anomaly, corresponds to emission due to domestic ruminants and other livestock [45]. In South America, high concentration anomalies are found over central eastern parts where livestock density is high. Over Europe, regions covering countries like France, Italy, Poland, Ukraine, etc. show high CH<sub>4</sub> anomalies (Figure 1a). Finland and western parts of Russia also show high anthropogenic CH<sub>4</sub> concentrations. The European sources are, mainly, extraction of fossil fuel, livestock and landfills, while East Asian sources are rice paddies, landfills and livestock [46]. In the past decade, coal mining has emerged as a significant source of methane in China, contributing around 40% of Chinese methane emissions [41]. Low concentrations in observed XCH<sub>4</sub> over elevated terrain (for example, over Tibetan Plateau and western United States) reflect in part a larger relative contribution of the stratospheric methane depletion to the column-average mixing ratio. (In the regression analysis, this bias has been adjusted by polynomial regression method—see Section 3.3).

A global list of locations having high XCH<sub>4</sub> anomaly is given in Table 1. Most of the locations are in East Asia. In Table 1, a number of locations where the simulated XCH<sub>4</sub> is greater than 10 ppb are listed. We can see that almost all of them are in Asian countries. Compared to the inventory estimates of XCH<sub>4</sub>, the observation derived anomalies are noisy (associated with each observation and even at spatial aggregations over small regions like 2° grids) (Figure 1b).

However, many locations characterized by high XCH<sub>4</sub> in simulations are also marked by high XCH<sub>4</sub> anomalies in observations as well. Mainly, pockets of high observed anomalies are seen over Asia, Europe, and South and North Americas, which match with the anthropogenic source regions in these regions, as also shown in more simple analysis by Buchwitz et al. [28]. Since the observed XCH<sub>4</sub> anomalies are noisy, a direct comparison with the simulated XCH<sub>4</sub> abundance is difficult. Therefore, aggregating these enhancements based on simulated abundance at equal intervals (2 ppb bins) over whole region helps reducing the spread in the data proportionally to the square root of the number of observations in each bin. The data uncertainty is estimated as single scan random error of 12.6 ppb (as established by GOSAT validation) divided by square root of observation number in each bin (Supplementary Materials).

To relate the observation-derived and inventory-based XCH<sub>4</sub> anomalies, after aggregating the enhancements in each 2 ppb bin based on simulated values, we fit a linear regression between them (i.e., observation derived enhancements as a function of simulated enhancements). The regression is carried out to a maximum XCH<sub>4</sub> abundance of 20 ppb only, considering the decreasing number of observations in each bin and the growing error in binned values (Figure S2). We examined large regions where anthropogenic methane emissions are large, based on information from bottom-up emission inventory. The large continental regions having significant emission from anthropogenic sources are North America, East Asia, Europe and the Middle East. In this analysis, we selected



North America and East Asia based on their contribution to global emissions and availability of large number of useful satellite observations. We have found good correlation between the observed and model simulated XCH<sub>4</sub> abundance due to anthropogenic activities over the globe, East Asia and North America. For the global case, the model–observation regression gives a regression coefficient (slope) of  $1.15 \pm 0.03$  ( $R^2 = 0.97$ ; Figure 2). The error in slope estimate includes both the uncertainty in the bin averages and departure of data from the regression fit. For East Asia, the regression slope is  $0.70 \pm 0.05$  ( $R^2 = 0.96$ ) and for North America it is  $1.28 \pm 0.01$  ( $R^2 = 0.65$ ; Figure 2). In our analysis, North American regions show the largest difference between the GOSAT observed and EDGAR based XCH<sub>4</sub> anomaly, compared to other regions. The regression slope shows around 28% deviation from unity. This shows a mismatch between observations based and inventory based XCH<sub>4</sub> anomalies over northern America and thereby a potential underestimation in the emission inventory. This result is in agreement with recent studies by Miller et al. [12] and Turner et al. [18] who showed anthropogenic CH<sub>4</sub> emission in North America is underestimated by 30–50%, attributable to oil and natural gas and livestock emissions. Over the East Asian region, the model–observation mismatch is approximately 30%, emission being higher than suggested by observation derived enhancements. This result is in agreement with recent studies by Thompson et al. [47] and Patra et al. [48]. The overestimation is reported to be in different source sectors over East Asia; for example, Turner et al. [15] have indicated that the Chinese coal emission of CH<sub>4</sub> is overrepresented in EDGARv4.2 by a factor of 2.

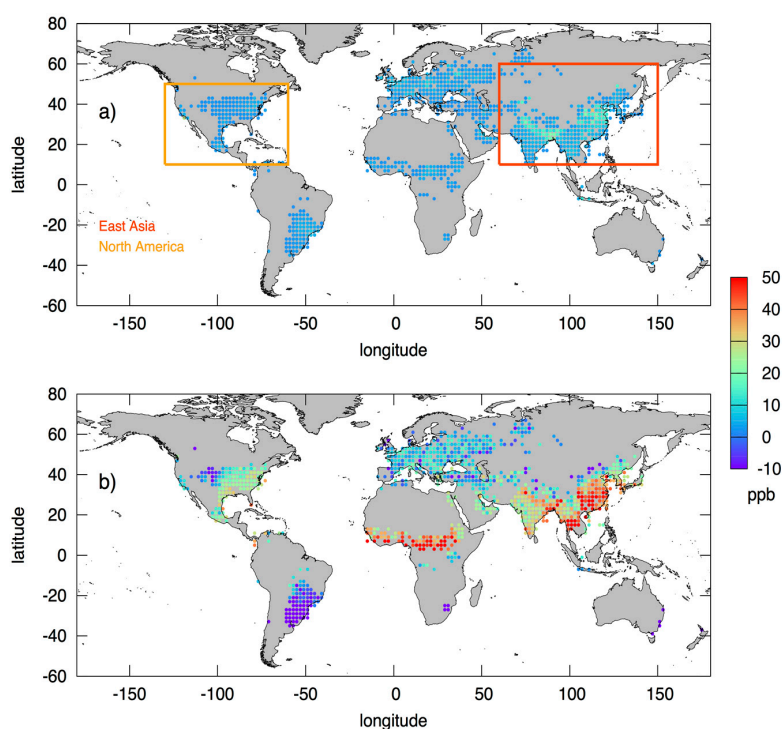


**Figure 1.** The simulated (a); and GOSAT observed (b) XCH<sub>4</sub> anomaly (ppb) ( $\Delta\text{XCH}_{4,\text{sim}}$  and  $\Delta\text{XCH}_{4,\text{obs}}$ , respectively) aggregated at 2° grid for a period 2009–2012. The grids with simulated XCH<sub>4</sub> abundance greater than 5 ppb in average are shown. The regions used in analysis are marked as rectangles in upper panel.

Finally, there is a concern that omission of some GOSAT observations from analysis may happen due to large underprediction of emissions by inventory or transport model errors. It should be noted that this analysis approach is not sensitive to emission underprediction in the order of 50% in relatively small fraction of grid points, as it would lead to effectively increasing detection threshold by a factor of 2 for those grid points. In the current setting, the threshold of 1 ppb allows detecting rather small

emissions, and number of omissions at lower emission range is expected to be small compared to the bulk of the data that contribute to regression analysis in the range of 0–20 ppb.

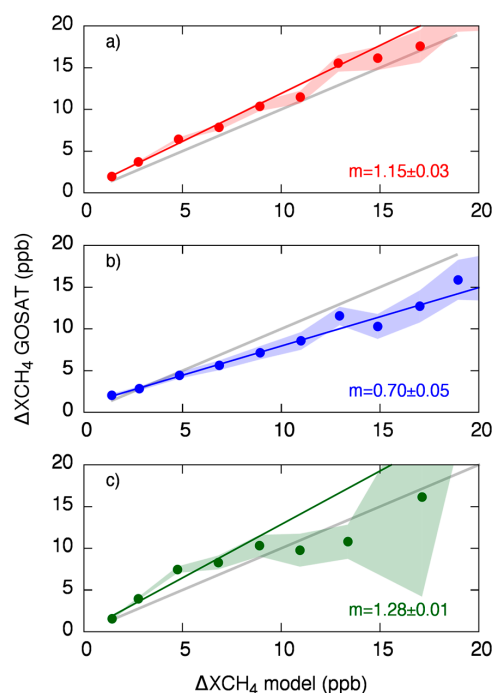


**Figure 2.** The regression between modeled (EDGAR,  $x$ -axis) and observed (GOSAT,  $y$ -axis)  $XCH_4$  abundance for: (a) the Globe; (b) East Asia; and (c) North America. The inset values ( $m$ ) are the regression coefficient (unit less) with the associated estimation error. The light shading represents the standard error in each bin. The colored lines show the regression model and the grey lines show the identity line.

**Table 1.** List of high  $XCH_4$  anomalies ( $>10$  ppb) simulated ( $\Delta XCH_{4,sim}$ ) and derived from GOSAT observations ( $\Delta XCH_{4,obs}$ ) over different regions over the globe averaged over  $2^\circ$  grid cells. The central latitude and longitude are given.

| Longitude (Degree) | Latitude (Degree) | $\Delta XCH_{4,obs}$ (ppb) | $\Delta XCH_{4,sim}$ (ppb) | Region                       |
|--------------------|-------------------|----------------------------|----------------------------|------------------------------|
| −119               | 33                | 21.39                      | 24.44                      | Los Angeles (USA)            |
| 73                 | 41                | 21.02                      | 13.88                      | Ferghana valley (Uzbekistan) |
| 77                 | 43                | 11.54                      | 13.20                      | Umnugovi (Mongolia)          |
| 105                | 31                | 58.47                      | 12.43                      | Ningxia (China)              |
| 107                | 31                | 55.30                      | 13.97                      | Dazhou (China)               |
| 107                | 35                | 18.63                      | 10.46                      | Baoji (China)                |
| 109                | 35                | 28.00                      | 11.27                      | Xian (China)                 |
| 111                | 35                | 14.01                      | 10.71                      | Yuncheng (China)             |
| 111                | 37                | 13.74                      | 17.16                      | Shanxi (China)               |
| 113                | 35                | 29.90                      | 20.67                      | Zhengzhou (China)            |
| 113                | 37                | 16.39                      | 40.80                      | Changzhi, Shanxi (China)     |
| 115                | 33                | 28.46                      | 16.39                      | Zhoukou, Fuyang (China)      |
| 115                | 35                | 26.59                      | 21.78                      | Puyang, Shangqiu (China)     |
| 117                | 33                | 23.49                      | 12.82                      | Bengbu (China)               |
| 117                | 39                | 22.13                      | 11.65                      | Tianjin (China)              |
| 119                | 31                | 42.80                      | 16.65                      | Xuancheng (China)            |
| 119                | 33                | 38.34                      | 11.93                      | Huai'an (China)              |
| 119                | 35                | 18.14                      | 16.20                      | Junan (China)                |
| 119                | 37                | 15.97                      | 20.48                      | Weifang, Dongying (China)    |
| 129                | 51                | 14.26                      | 13.82                      | Belogorsk (Russia)           |

## 5. Conclusions

In this study, we present a method to extract the information on anthropogenic methane emissions from the global observations of  $\text{XCH}_4$  by GOSAT. Using a high resolution transport model with anthropogenic methane emission inventory, we calculate the  $\text{XCH}_4$  abundance at GOSAT  $\text{XCH}_4$  observation locations over the globe for 2009–2012. Using these inventory based estimates, we select the GOSAT  $\text{XCH}_4$  observations influenced by emission from anthropogenic sources, where the threshold for marking observations as polluted is 1 ppb in simulated value ( $\text{XCH}_{4,\text{sim}}$ ).  $\text{XCH}_4$  anomalies due to anthropogenic sources are calculated as the departure of each observation from clean background value. The pair of  $\text{XCH}_4$  abundance thus obtained from observations and simulations were aggregated in 2 ppb bins and compared. The aggregation into bins helps overcome the limitation of error associated with each observation and reduces the influence of noise to observations. The paired data thus obtained over a given region and time, when subjected to error weighted linear regression analysis, give a scaling factor between the observation and inventory based  $\text{XCH}_4$  abundance, which will be indicative of the potential biases in the bottom-up inventories. Using this method, we can establish a linear relation between the observation-derived  $\text{XCH}_4$  abundance due to anthropogenic sources and those calculated using bottom-up inventories over large regions. In this analysis, we have found linear relations between the model and observation over the analysis regions but have opposite biases in bottom-up emissions over East Asian and North American regions. A significant difference of about 28% (emission underrepresented in inventory) between the observed  $\text{XCH}_4$  abundance and inventory-based estimates is found over North American continent. This is consistent with other studies using inversion with satellite and ground-based methane observations. Over East Asia, anthropogenic methane emission is overestimated in the inventory by approximately 30% as suggested by the regression slope of that region, as has been reported by recent studies. Therefore, given large number of GOSAT observations over a region and time, this statistical technique could be a promising tool for methane emission verification at regional scales using GOSAT observations.

**Supplementary Materials:** The following are available online at [www.mdpi.com/2072-4292/9/9/941/s1](http://www.mdpi.com/2072-4292/9/9/941/s1), Figure S1: Dependence of  $\text{XCH}_4$  on terrain height over various analysis domains. Figure S2: Number of GOSAT  $\text{XCH}_4$  observations used in each 2 ppb bin and the associated standard errors. Figure S3: Percentage difference of EDGAR  $\text{CH}_4$  emission for 2010 and that prepared for the same year by scaling 2009 emission by global total reported by EDGAR.

**Acknowledgments:** We thank the reviewers for their insightful comments and suggestions to improve this paper. The authors are grateful to the GOSAT project at the National Institute for Environmental Studies, Tsukuba, Japan, for support and providing the GOSAT Level 2  $\text{XCH}_4$  data. The simulations are carried out using the supercomputer facility and GOSAT Research Computation Facility at the National Institute for Environmental Studies. The study was also supported by Environment Research and Technology Development Fund (grant 2-1401), Ministry of Environment, Japan.

**Author Contributions:** Shamil Maksyutov and Rajesh Janardanan designed the study and wrote the paper; Rajesh Janardanan did the simulation experiments and analyzed the data; Yoshida Yukio and Tsuneo Matsunaga provided the  $\text{XCH}_4$  observations; Akihiko Ito discussed the natural variability of methane flux as well as the results and revised the manuscript; all the authors discussed the results and contributed to the manuscript.

**Conflicts of Interest:** The authors declare no conflict of interest.

## References

1. Intergovernmental Panel on Climate Change (IPCC). Climate Change 2013: The Physical Science Basis, Working Group I Contribution to the Fifth Assessment Report of the Intergovernmental Report on Climate Change. 2013. Available online: <http://www.ipcc.ch/report/ar5/wg1/> (accessed on 1 September 2017).
2. Saunio, M.; Bousquet, P.; Poulter, B.; Peregon, A.; Ciais, P.; Canadell, J.G.; Dlugokencky, E.J.; Etiope, G.; Bastviken, D.; Houweling, S.; et al. The Global Methane Budget: 2000–2012. *Earth Syst. Sci. Data* **2016**, *8*, 697–751. [[CrossRef](#)]
3. Hansen, J.; Sato, M. Greenhouse gas growth rates. *Proc. Natl. Acad. Sci. USA* **2004**, *101*, 16109–16114. [[CrossRef](#)] [[PubMed](#)]



4. Etheridge, D.M.; Steele, L.P.; Francey, R.J.; Langenfelds, R.L. Atmospheric methane between 1000 A.D. and present: Evidence of anthropogenic emissions and climatic variability. *J. Geophys. Res.* **1998**, *103*, 15979–15993. [[CrossRef](#)]
5. Dlugokencky, E.J.; Bruhwiler, L.; White, J.W.C.; Emmons, L.K.; Novelli, P.C.; Montzka, S.A.; Masarie, K.A.; Lang, P.M.; Crotwell, A.M.; Miller, J.B.; et al. Observational constraints on recent increases in the atmospheric CH<sub>4</sub> burden. *Geophys. Res. Lett.* **2009**, *36*, L18803. [[CrossRef](#)]
6. Kirschke, S.; Bousquet, P.; Ciais, P.; Saunio, M.; Canadell, J.G.; Dlugokencky, E.J.; Bergamaschi, P.; Bergmann, D.; Blake, D.R.; Bruhwiler, L.; et al. Three decades of global methane sources and sinks. *Nat. Geosci.* **2013**, *6*, 813–823. [[CrossRef](#)]
7. Checa-Garcia, R.; Shine, K.P.; Hegglin, M.I. The contribution of greenhouse gases to the recent slowdown in global-mean temperature trends. *Environ. Res. Lett.* **2016**, *11*, 094018. [[CrossRef](#)]
8. Saunio, M.; Jackson, R.B.; Bousquet, P.; Poulter, B.; Canadell, J.G. The growing role of methane in anthropogenic climate change. *Environ. Res. Lett.* **2016**, *11*, 120207. [[CrossRef](#)]
9. Rigby, M.; Montzka, S.A.; Prinn, R.G.; White, J.W.C.; Young, D.; O'Doherty, S.; Lunt, M.F.; Ganesan, A.L.; Manning, A.J.; Simmonds, P.G.; et al. Role of atmospheric oxidation in recent methane growth. *Proc. Natl. Acad. Sci. USA* **2017**, *114*, 5373–5377. [[CrossRef](#)] [[PubMed](#)]
10. Nisbet, E.G.; Dlugokencky, E.J.; Manning, M.R.; Lowry, D.; Fisher, R.E.; France, J.L.; Michel, S.E.; Miller, J.B.; White, J.W.C.; Vaughn, B.; et al. Rising atmospheric methane: 2007–2014 growth and isotopic shift. *Glob. Biogeochem. Cycles* **2016**, *30*, 1356–1370. [[CrossRef](#)]
11. Turner, A.J.; Jacob, D.J.; Benmergui, J.; Wofsy, S.C.; Maasakkers, J.D.; Butz, A.; Hasekamp, O.; Biraud, S.C. A large increase in U.S. methane emissions over the past decade inferred from satellite data and surface observations. *Geophys. Res. Lett.* **2016**, *43*, 2218–2224. [[CrossRef](#)]
12. Miller, S.M.; Wofsy, S.C.; Michalak, A.M.; Kort, E.A.; Andrews, A.E.; Biraud, S.C.; Dlugokencky, E.J.; Eluszkiewicz, J.; Fischer, M.L.; Janssens-Maenhout, G.; et al. Anthropogenic emissions of methane in the United States. *Proc. Natl. Acad. Sci. USA* **2013**, *110*, 20018–20022. [[CrossRef](#)] [[PubMed](#)]
13. McKain, K.; Down, A.; Raciti, S.M.; Budney, J.; Huttyra, L.R.; Floerchinger, C.; Herndon, S.C.; Nehrkorn, T.; Zahniser, M.S.; Jackson, R.B.; et al. Methane emissions from natural gas infrastructure and use in the urban region of Boston, Massachusetts. *Proc. Natl. Acad. Sci. USA* **2015**, *112*, 1941–1946. [[CrossRef](#)] [[PubMed](#)]
14. Zavala-Araiza, D.; Lyon, D.R.; Alvarez, R.A.; Davis, K.J.; Harriss, R.; Herndon, S.C.; Karion, A.; Kort, E.A.; Lamb, B.K.; Lan, X.; et al. Reconciling divergent estimates of oil and gas methane emissions. *Proc. Natl. Acad. Sci. USA* **2015**, *112*, 15597–15602. [[CrossRef](#)] [[PubMed](#)]
15. Henne, S.; Brunner, D.; Oney, B.; Leuenberger, M.; Eugster, W.; Bamberger, I.; Meinhardt, F.; Steinbacher, M.; Emmenegger, L. Validation of the Swiss methane emission inventory by atmospheric observations and inverse modelling. *Atmos. Chem. Phys.* **2016**, *16*, 3683–3710. [[CrossRef](#)]
16. Karion, A.; Sweeney, C.; Kort, E.A.; Shepson, P.B.; Brewer, A.; Cambaliza, M.; Conley, S.A.; Davis, K.; Deng, A.; Hardesty, M.; et al. Aircraft-Based Estimate of Total Methane Emissions from the Barnett Shale Region. *Environ. Sci. Technol.* **2015**, *49*, 8124–8131. [[CrossRef](#)] [[PubMed](#)]
17. Maasakkers, J.D.; Jacob, D.J.; Sulprizio, M.P.; Turner, A.J.; Weitz, M.; Wirth, T.; Hight, C.; DeFigueiredo, M.; Desai, M.; Schmeltz, R.; et al. Gridded National Inventory of U.S. Methane Emissions. *Environ. Sci. Technol.* **2016**, *50*, 13123–13133. [[CrossRef](#)] [[PubMed](#)]
18. Turner, A.J.; Jacob, D.J.; Wecht, K.J.; Maasakkers, J.D.; Lundgren, E.; Andrews, A.E.; Biraud, S.C.; Boesch, H.; Bowman, K.W.; Deutscher, N.M.; et al. Estimating global and North American methane emissions with high spatial resolution using GOSAT satellite data. *Atmos. Chem. Phys.* **2015**, *15*, 7049–7069. [[CrossRef](#)]
19. Bousquet, P.; Ciais, P.; Miller, J.B.; Dlugokencky, E.J.; Hauglustaine, D.A.; Prigent, C.; Van der Werf, G.R.; Peylin, P.; Brunke, E.-G.; Carouge, C.; et al. Contribution of anthropogenic and natural sources to atmospheric methane variability. *Nature* **2006**, *443*, 439–443. [[CrossRef](#)] [[PubMed](#)]
20. Bergamaschi, P.; Krol, M.; Meirink, J.F.; Dentener, F.; Segers, A.; Van Aardenne, J.; Monni, S.; Vermeulen, A.T.; Schmidt, M.; Ramonet, M.; et al. Inverse modeling of European CH<sub>4</sub> emissions 2001–2006. *J. Geophys. Res. Atmos.* **2010**, *115*, D22309. [[CrossRef](#)]
21. Parker, R.J.; Boesch, H.; Wooster, M.J.; Moore, D.P.; Webb, A.J.; Gaveau, D.; Murdiyarso, D. Atmospheric CH<sub>4</sub> and CO<sub>2</sub> enhancements and biomass burning emission ratios derived from satellite observations of the 2015 Indonesian fire plumes. *Atmos. Chem. Phys.* **2016**, *16*, 10111–10131. [[CrossRef](#)]

22. Yokota, T.; Yoshida, Y.; Eguchi, N.; Ota, Y.; Tanaka, T.; Watanabe, H.; Maksyutov, S. Global Concentrations of CO<sub>2</sub> and CH<sub>4</sub> Retrieved from GOSAT: First Preliminary Results. *Sola* **2009**, *5*, 160–163. [[CrossRef](#)]
23. Yoshida, Y.; Kikuchi, N.; Morino, I.; Uchino, O.; Oshchepkov, S.; Bril, A.; Saeki, T.; Schutgens, N.; Toon, G.C.; Wunch, D.; et al. Improvement of the retrieval algorithm for GOSAT SWIR XCO<sub>2</sub> and XCH<sub>4</sub> and their validation using TCCON data. *Atmos. Meas. Tech.* **2013**, *6*, 1533–1547. [[CrossRef](#)]
24. Kuze, A.; Suto, H.; Nakajima, M.; Hamazaki, T. Thermal and near infrared sensor for carbon observation Fourier-transform spectrometer on the Greenhouse Gases Observing Satellite for greenhouse gases monitoring. *Appl. Opt.* **2009**, *48*, 6716–6733. [[CrossRef](#)] [[PubMed](#)]
25. Kort, E.A.; Frankenberg, C.; Costigan, K.R.; Lindenmaier, R.; Dubey, M.K.; Wunch, D. Four corners: The largest US methane anomaly viewed from space. *Geophys. Res. Lett.* **2014**, *41*, 6898–6903. [[CrossRef](#)]
26. Janardanan, R.; Maksyutov, S.; Oda, T.; Saito, M.; Kaiser, J.W.; Ganshin, A.; Stohl, A.; Matsunaga, T.; Yoshida, Y.; Yokota, T. Comparing GOSAT observations of localized CO<sub>2</sub> enhancements by large emitters with inventory-based estimates. *Geophys. Res. Lett.* **2016**, *43*, 3486–3493. [[CrossRef](#)]
27. Hakkarainen, J.; Ialongo, I.; Tamminen, J. Direct space-based observations of anthropogenic CO<sub>2</sub> emission areas from OCO-2. *Geophys. Res. Lett.* **2016**, *43*, 11400–11406. [[CrossRef](#)]
28. Buchwitz, M.; Schneising, O.; Reuter, M.; Heymann, J.; Krautwurst, S.; Bovensmann, H.; Burrows, J.P.; Boesch, H.; Parker, R.J.; Detmers, R.G.; et al. Satellite-derived methane hotspot emission estimates using a fast data-driven method. *Atmos. Chem. Phys.* **2017**, *17*, 5751–5774. [[CrossRef](#)]
29. Bovensmann, H.; Buchwitz, M.; Burrows, J.P.; Reuter, M.; Krings, T.; Gerilowski, K.; Schneising, O.; Heymann, J.; Tretner, A.; Erzinger, J. A remote sensing technique for global monitoring of power plant CO<sub>2</sub> emissions from space and related applications. *Atmos. Meas. Tech.* **2010**, *3*, 781–811. [[CrossRef](#)]
30. Heymann, J.; Reuter, M.; Buchwitz, M.; Schneising, O.; Bovensmann, H.; Burrows, J.P.; Massart, S.; Kaiser, J.W.; Crisp, D. CO<sub>2</sub> emission of Indonesian fires in 2015 estimated from satellite-derived atmospheric CO<sub>2</sub> concentrations. *Geophys. Res. Lett.* **2017**, *44*, 1537–1544. [[CrossRef](#)]
31. Olivier, J.G.J.; Janssens-Maenhout, G. CO<sub>2</sub> Emissions From Fuel Combustion (2012 Edition): Part III: Greenhouse-Gas Emissions; IEA: Paris, France, 2012; ISBN 978-92-64-17475-7.
32. Ito, A.; Inatomi, M. Use of a process-based model for assessing the methane budgets of global terrestrial ecosystems and evaluation of uncertainty. *Biogeosciences* **2012**, *9*, 759–773. [[CrossRef](#)]
33. Onogi, K.; Tsutsui, J.; Koide, H.; Sakamoto, M.; Kobayashi, S.; Hatsushika, H.; Matsumoto, T.; Yamazaki, N.; Kamahori, H.; Takahashi, K.; et al. The JRA-25 Reanalysis. *J. Meteorol. Soc. Jpn. Ser. II* **2007**, *85*, 369–432. [[CrossRef](#)]
34. Stohl, A.; Hittenberger, M.; Wotawa, G. Validation of the lagrangian particle dispersion model FLEXPART against large-scale tracer experiment data. *Atmos. Environ.* **1998**, *32*, 4245–4264. [[CrossRef](#)]
35. Stohl, A.; Forster, C.; Frank, A.; Seibert, P.; Wotawa, G. Technical note: The Lagrangian particle dispersion model FLEXPART version 6.2. *Atmos. Chem. Phys.* **2005**, *5*, 2461–2474. [[CrossRef](#)]
36. Brown, J.D. *Linear Models in Matrix Form-A Hands-On Approach for the behavioral Sciences*; Springer International Publishing: Cham, Switzerland, 2014; ISBN 978-3-319-11733-1.
37. Ganshin, A.; Oda, T.; Saito, M.; Maksyutov, S.; Valsala, V.; Andres, R.J.; Fisher, R.E.; Lowry, D. A global coupled Eulerian-Lagrangian model and 1 × 1 km CO<sub>2</sub> surface flux dataset for high-resolution atmospheric CO<sub>2</sub> transport simulations. *Geosci. Model Dev.* **2012**, *5*, 231–243. [[CrossRef](#)]
38. Seibert, P.; Frank, A. Source-receptor matrix calculation with a Lagrangian particle dispersion model in backward mode. *Atmos. Chem. Phys.* **2004**, *4*, 51–63. [[CrossRef](#)]
39. Nakazawa, T.; Aoki, S.; Kawamura, K.; Saeki, T.; Sugawara, S.; Honda, H.; Hashida, G.; Morimoto, S.; Yoshida, N.; Toyoda, S.; et al. Variations of stratospheric trace gases measured using a balloon-borne cryogenic sampler. *Adv. Space Res.* **2002**, *30*, 1349–1357. [[CrossRef](#)]
40. Huang, Y.; Zhang, W.; Zheng, X.; Han, S.; Yu, Y. Estimates of methane emissions from Chinese rice paddies by linking a model to GIS database. *Acta Ecol. Sin.* **2006**, *26*, 980–987. [[CrossRef](#)]
41. Peng, S.; Piao, S.; Bousquet, P.; Ciais, P.; Li, B.; Lin, X.; Tao, S.; Wang, Z.; Zhang, Y.; Zhou, F. Inventory of anthropogenic methane emissions in mainland China from 1980 to 2010. *Atmos. Chem. Phys.* **2016**, *16*, 14545–14562. [[CrossRef](#)]
42. Garg, A.; Kankal, B.; Shukla, P.R. Methane emissions in India: Sub-regional and sectoral trends. *Atmos. Environ.* **2011**, *45*, 4922–4929. [[CrossRef](#)]

43. Robinson, T.P.; Wint, G.R.W.; Conchedda, G.; Van Boeckel, T.P.; Ercoli, V.; Palamara, E.; Cinardi, G.; D'Aiotti, L.; Hay, S.I.; Gilbert, M. Mapping the Global Distribution of Livestock. *PLoS ONE* **2014**, *9*, e96084. [[CrossRef](#)] [[PubMed](#)]
44. Yamaji, K.; Ohara, T.; Akimoto, H. Regional-specific emission inventory for  $\text{NH}_3$ ,  $\text{N}_2\text{O}$ , and  $\text{CH}_4$  via animal farming in South, Southeast, and East Asia. *Atmos. Environ.* **2004**, *38*, 7111–7121. [[CrossRef](#)]
45. Herrero, M.; Thornton, P.K.; Kruska, R.; Reid, R.S. Systems dynamics and the spatial distribution of methane emissions from African domestic ruminants to 2030. *Agric. Ecosyst. Environ.* **2008**, *126*, 122–137. [[CrossRef](#)]
46. Xiao, Y.; Jacob, D.J.; Wang, J.S.; Logan, J.A.; Palmer, P.I.; Suntharalingam, P.; Yantosca, R.M.; Sachse, G.W.; Blake, D.R.; Streets, D.G. Constraints on Asian and European sources of methane from  $\text{CH}_4$ - $\text{C}_2\text{H}_6$ -CO correlations in Asian outflow. *J. Geophys. Res. Atmos.* **2004**, *109*, D15S16. [[CrossRef](#)]
47. Thompson, R.L.; Stohl, A.; Zhou, L.X.; Dlugokencky, E.; Fukuyama, Y.; Tohjima, Y.; Kim, S.Y.; Lee, H.; Nisbet, E.G.; Fisher, R.E.; et al. Methane emissions in East Asia for 2000–2011 estimated using an atmospheric Bayesian inversion. *J. Geophys. Res. Atmos.* **2015**, *120*, 4352–4369. [[CrossRef](#)]
48. Patra, P.K.; Saeki, T.; Dlugokencky, E.J.; Ishijima, K.; Umezawa, T.; Ito, A.; Aoki, S.; Morimoto, S.; Kort, E.A.; Crowell, A.; et al. Regional Methane Emission Estimation Based on Observed Atmospheric Concentrations (2002–2012). *J. Meteorol. Soc. Jpn. Ser. II* **2016**, *94*, 91–113. [[CrossRef](#)]



© 2017 by the authors. Licensee MDPI, Basel, Switzerland. This article is an open access article distributed under the terms and conditions of the Creative Commons Attribution (CC BY) license (<http://creativecommons.org/licenses/by/4.0/>).